Article

High-resolution microstructure characterization of additively manufactured X5CrNiCuNb17-4 maraging steel during *ex* and *in situ* thermal treatment

Mihaela Albu[1*], Bernd Panzirsch[2], Hartmuth Schröttner[3], Stefan Mitsche[3], Klaus Reichmann[4], Cecilia Poletti[5] and Gerald Kothleitner[1,3]

[1] Graz Centre for Electron Microscopy, Steyrergasse 17, 8010 Graz; mihaela.albu@felmi-zfe.at
[2] ÖGI- Austrian Foundry Institute, Parkstraße 21, 8700 Leoben, Österreich; bernd.panzirsch@ogi.at
[3] Institute of Electron Microscopy and Nanoanalysis, TU Graz, Steyrergasse 17, 8010 Graz; hartmuth.schroettner@felmi-zfe.at, stefan.mitsche@felmi-zfe.at, Gerald.kothleitner@felmi-zfe.at
[4] Institute for Chemistry and Technology of Materials, TU Graz, Stremayrgasse 9, 8010 Graz; k.reichmann@tugraz.at
[5] Institute of Materials Science, Joining and Forming, TU Graz, Kopernikusgasse 24, 8010 Graz; cecilia.poletti@tugraz.at
* Correspondence: mihaela.albu@felmi-zfe.at; Tel.: +43 316 873 8348

Abstract: Powder and SLM additively manufactured parts of X5CrNiCuNb17-4 maraging steel were systematically investigated by electron microscopy to understand the relationship between the properties of the powder grains and the microstructure of the printed parts. We prove that satellites, irregularities and superficial oxidation of powder particles can be transformed into an advantage through the formation of nanoscale (AlMnSiTiCr)-oxides in the matrix during the printing process. The nano-oxides showed extensive stability in terms of size, spherical morphology, chemical composition and crystallographic disorder upon *in situ* heating up to 950°C in the scanning transmission electron microscope. Their presence thus indicates a potential for oxide-dispersive strengthening of this steel, which may be beneficial for creep resistance at elevated temperatures. The nucleation of copper clusters and their evolution into nanoparticles as well as the precipitation of Ni and Cr particles upon *in situ* heating have as well been systematically documented.

Keywords: additive manufacturing; microstructure; STEM *in situ* heating experiments

1. Introduction

Maraging steels are low carbon precipitation hardenable martensitic steels with high strength and toughness, high temperature creep resistance and low temperature properties but also corrosion resistant. These properties qualify them as promising steels for structural applications and also as favorites for additive manufacturing due to their very good weldability. Few types of steels are actually used for additively manufactured components with complex geometries in aerospace, automobile, medical techniques, tooling and other industry applications: austenitic stainless steels (AlSl-316L/1.4404, AlSl-304/1.4307), duplex stainless steel (SAF2 705), maraging steels (17-4PH/1.4542, 15-5PH/1.4545, 18PH-300/1.2709), and C-bearing (H13) tool steel as well as oxide dispersive steels (PM2000) [1-5]. The steels are selected based on application areas for which the additively manufactured components should perform high corrosion resistance and long service lifetimes in extreme conditions, enhanced mechanical properties (strenghts, ductility, hardness, toughness, wear resistance, etc.), multivalent microstructural properties (from hard martensite to ductile multiphase components), different functionalities (electromagnetic or invar properties) and, of course, an affordable price to make it attractive for the industry [5].

 doi:10.20944/preprints202111.0356.v1

The microstructure of additively produced maraging steels in the "as-built" condition is refined due to the high cooling rates the material experiences, and consists of few small retained austenite grains mixed with dislocation-rich ferritic / martensitic (bcc) laths. In addition, depending on the printing parameters and powder characteristics (e.g. uniformity of grain size and natural surface oxidation) element segregations and rather large oxide inclusions (TiO2:Al2O3 of about 10 – 20 μm, or other oxides containing Ti, Mo, Al and Si in various ratios) [4] have been observed at melt pool boundaries. Their presence, by consistently high density of the part (absence of pores), is however, generally considered to have an unfavorable influence on the mechanical properties of the printed part [4-6] because of crack initiation. On the other hand, the *in situ* addition during the additive production of dispersive oxide (ODS) powders [7,8] or the use of environmental oxygen or nitrogen gases to form ODS (TixOy, AlyOy) or nitrogen dispersed particles (NDS) during printing, induced a significant increase in hardness and thermal stability [9]. However, such uniformly dispersed oxides with dimensions in the nanometer and micrometer range have been detected only by few authors [10-14] in additively manufactured (L-PBF) stainless and maraging steels.

Most stainless and maraging steels uses intermetallic compounds precipitation at temperatures between 400 and 650°C as strengthening mechanism [15]. These precipitates with sizes between 50 nm and 1 μm form at laths interfaces and are expected to impede the movement of subgrains and dislocations (through the Orowan effect), thus contributing to the precipitation hardening. However, thermal stability of the precipitates at elevated temperatures is critical to resist grain growth and dislocation recovery when long-term creep strength of the printed components needs to be achieved.

This work provides a detailed microstructure study of the X5CrNiCuNb17-4 precipitation hardened stainless steel [1,16], in powder form as well as additively manufactured by selective laser melting in the as-built condition and heat treated according to the recommended scheme that also applies to the bar material (H1150 (620°C): [P930]). This grade contains Cr and Ni for corrosion resistance and Cu for precipitation hardening (fcc - nano-precipitates) that is achieved upon ageing heat treatment [1,16-18].

By studying the samples in a high-resolution scanning transmission electron microscope (STEM) using *in situ* thermal treatment and correlation with simultaneous thermal analysis (STA) measurements, we aim to understand the relationship between the powder characteristics and the microstructural details that might influence the properties of the printed parts. In particular, we systematically followed the evolution of the nanometric spherical oxides as well as the chromium and copper precipitate nucleation and coarsening upon heating of the sample in the as-built condition up to 950°C. Such experiments have, to the best of our knowledge, only been reported for AlSi10Mg alloy [19].

2. Materials and Methods

The microstructure of the X5CrNiCuNb17-4 steel in powder form and additively manufactured in as-built condition as well as the thermally treated specimen (1040°C/30min/air cooling + 620°C/4h/air cooling) have been extensively investigated by optical, scanning and high-resolution transmission electron microscopy techniques as well as simultaneous thermal analysis. For both samples we measured the hardness (replacing the tensile test) and determine the fatigue strength by nanoindentation technique.

The spherical powder was produced by argon gas atomization and has a broad particle size distribution between 14 and 45μm (D10[μm] 18 – 24, D50[μm] 29 – 35, D90[μm] 42 – 50) [16,20]. The cycled powder (mixture of pristine and the excess of a previous printing) was used for additive manufacturing by selective laser melting. The chemical compositions of the powder and of the additively manufactured sample in the as-built condition, as determined by wet chemical analysis, are listed in Table 1. The

Preprints (www.preprints.org) | NOT PEER-REVIEWED | Posted: 19 November 2021 doi:10.20944/preprints202111.0356.v1

chemical composition of the as-built sample differs slightly from the powder, indicating that some elements (C, Si, Mn, Nb, Mo) were evaporated during the printing process. After thermal treatment, the chemical composition remained unchanged. The printing parameters for the as-built sample are given in Table 2.

Table 1. Chemical composition of the powder [1,16] and as-built condition (wt. %). The standard deviation of the measurement lies between 3 - 5 %.

wt. %	C	Si	Mn	Cr	Ni	Cu	Nb	P	S	Mo	Fe
Powder [1]	0.07	0.7	1.0	15 - 17	3 - 5	3 - 5	0.45	0.025	0.015	0.5	bal.
as-built	0.04	0.34	0.36	15.2	4.80	3.03	0.25	0.02	0.006	0.26	bal.

Table 2. Printing parameters of the X5CrNiCuNb17-4 steel.

Power	Speed	Hatch distance	Layer Thickness
250 W	850 mm/s	0.1 mm	0.05 mm

The X5CrNiCuNb17-4 powder, as-built and thermally treated samples were first examined in a scanning electron microscope (SEM). An adhesive tape was used to pick up the powder grains for morphology and sphericity analysis. A second batch of the powder was embedded in a resin (CALDOFIX), polished down to a few tenths of a micrometer, and thinned by Ar -ion milling at cryogenic temperature. The additively manufactured samples were cut and polished along the build direction (z-axis) and the basal plane (xy-plane), using diamond and aluminum suspensions as final polishing steps for electron backscatter diffraction (EBSD) measurements. SEM micrographs were acquired using backscatter, secondary electron, and in-lens detectors. We used energy dispersive X-ray spectrometry for the analytical studies and EBSD for crystallographic studies of the grains and grain boundaries.

The *ex situ* samples for scanning transmission electron microscopy (STEM) analysis were prepared by Ar ion milling at cryogenic temperature, while for the *in situ* heating experiments, a focused ion beam (FIB) prepared lamella, cut from the as-built sample, was mounted on a MEMS heating chip (DENS solutions-Wildfire H+ DT, heating/quenching rate 200°C/ms and settling time 2s). For the high-resolution STEM studies, we used a probe-corrected microscope FEI Titan G3 60-300 (Thermo Fisher GmbH) operated at 300kV. HR-STEM micrographs were acquired using the annular (ADF) and high angle annular dark field (HAADF) detectors. Analytical studies were performed using energy dispersive X-ray analysis (EDS) and electron energy loss spectroscopies. For EDS the microscope is equipped with a windowless silicon drift detector FEI Super-X (Chemi-STEM technology) and for electron energy loss spectroscopy with a dual EELS Quantum Gatan Imaging Filter (GIF).

The nanoindentation measurements were performed using the NHT3 Nanointender from Anton Paar. Each sample was tested in all three regions of the stepwise geometry presented in Fig. 2a.

Simultaneous Thermal Analyses (STA) combining thermogravimetry (TG) and differential scanning calorimetry (DSC) were performed in a NETZSCH STA 449F1 Jupiter in Argon atmosphere applying different heating and cooling rates.

3. Results

The morphology, chemical composition, particle size distribution, and roundness factor of the X5CrNiCuNb17-4 powder grains have been studied in detail and published elsewhere [1, 20].

We observed a rather large size distribution and a high amount of satellites. STEM Analysis of a focused ion beam lamella cut from such a grain with satellites and accretionary forms (Fig. 1a and b) revealed the presence of Ni-intermetallic phases (Fig. 1c #1) and Cu-metallic layers (Fig. 1c #2) as well as a nm-thin layer of amorphous carbon at the interface between the particle body and the accretionary envelope (Fig. 1c #3).

Preprints (www.preprints.org) | NOT PEER-REVIEWED | Posted: 19 November 2021 doi:10.20944/preprints202111.0356.v1

Furthermore a 10 nm thin passive oxide layer was found to cover the particles and irregularities.

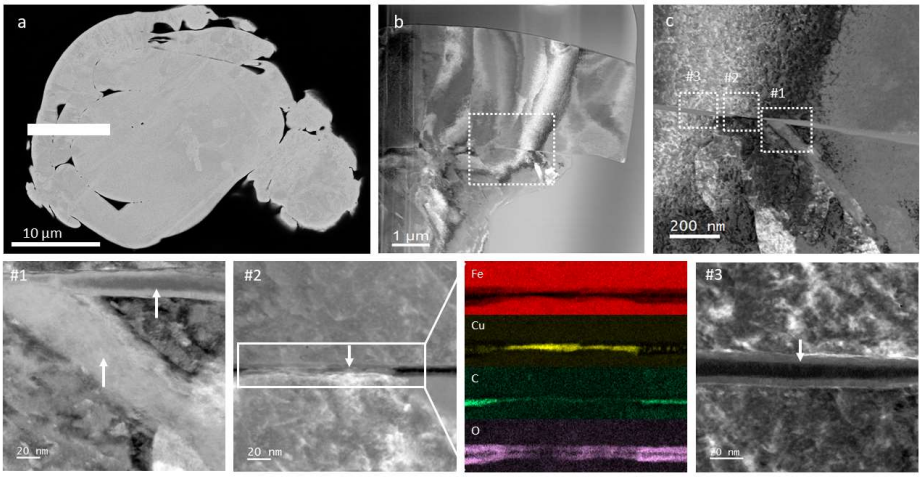

Figure 1. Powder characterization by SEM and STEM. a) SEM of a corrupted particle with the FIB lamella position; b) STEM ADF image of the FIB lamella; c) STEM HAADF image at higher magnification. The insets #1, #2 and #3 represent different regions at the interface of the particle body with the envelope. #1 – Ni intermetallic phases, #2 – Cu metallic interface and #3 – amorphous C and iron oxides. The Fe, Cu, C, and O - EDX maps reveal the interface from area #2.

The geometry of the printed samples was stepwise (Fig. 2a) to determine the effect of redundant heat during the printing process on the microstructure and mechanical properties. The mechanical properties for the as-built sample and the thermally treated sample (1050°C / 3min / air + 620°C / 4h / air), measured by nanoindentation, are presented in Fig. 2b. The measurement for all three areas showed low influence of the thermal treatment on the nanohardness.

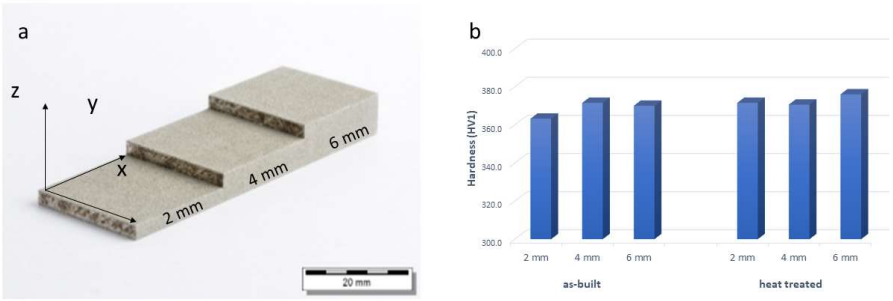

Figure 2. a) Image of the printed sample with the step-wise geometry; b) nanoindentation measurements performed for the as-built and heat-treated samples for the three areas with different thicknesses (2, 4 and 6 mm).

The as-built sample was extensively investigated in the build-up direction (z-axis) as well as in the basal plane (xy-plane) by means of optical microscopy and scanning electron microscopy (Fig. 3). The SEM images show distinct areas of microsegregation, which can be attributed to the quick cooling and solidification during the laser process. The microsegregations occur in lines at the interface between the melt pools - following the layers - and have a reduced hardness to the matrix, so they could serve as preferential crack paths. Their chemical analyses by EDX showed a mixture of Ni, Mo, Ti, Nb, W with various concentrations.

Preprints (www.preprints.org) | NOT PEER-REVIEWED | Posted: 19 November 2021 doi:10.20944/preprints202111.0356.v1

EBSD analysis showed a fine microstructure with small austenite grains of 280 to 340 nm in size, mixed with larger ferrite and martensite grains of about 10 µm (Fig. 3g - j). The austenite fraction, as quantified from the EBSD images in both z-direction and xy plane, ranged from 2 to 3.1 %. No clear columnar grains of increased size were observed in the heat-affected zones at the boundaries of the melt pools, indicating that the printing parameters were optimized for the best homogeneous microstructure that a sample can have in the as-built condition.

At higher magnifications, we noticed micrometer-sized pores and dark or bright small spherical features.

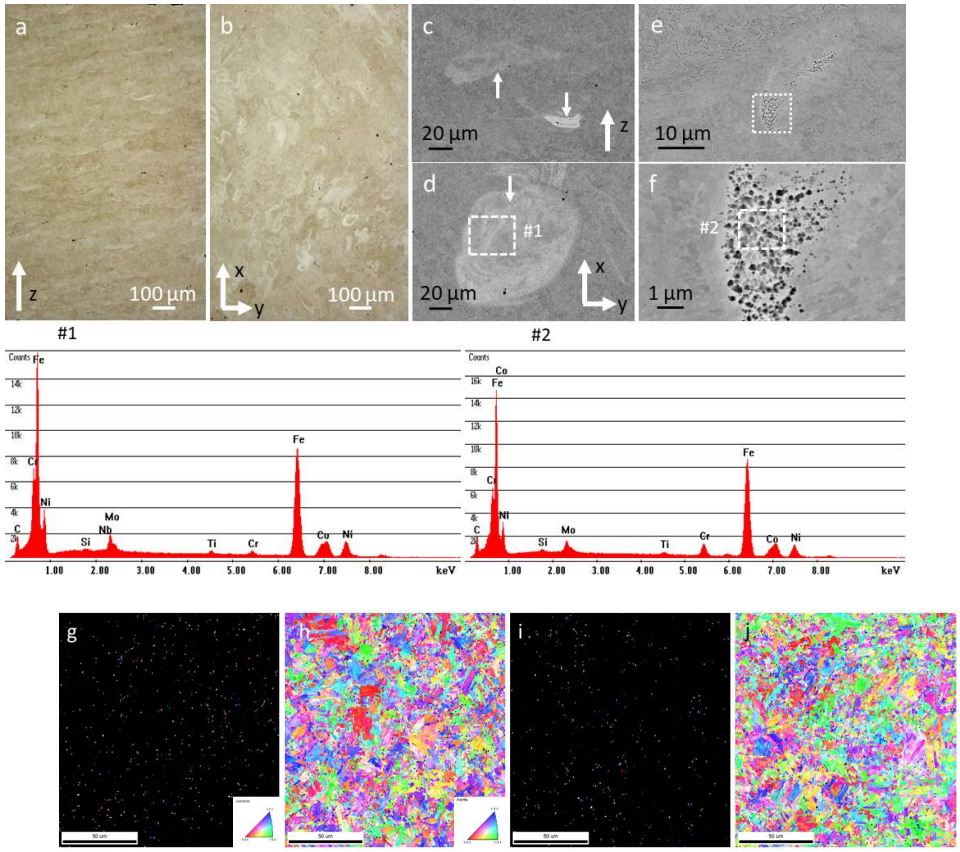

Figure 3. As-built sample characterization by optical microscopy (Infinite Focus Microscope) and SEM. a) IFM of the sample polished in the build direction (z-axis) and b) in the basal plane; c) and d) SEM of the as-built sample in the build direction (z-axis) and basal plane with the EDX spectrum #1 from a microsegregation area; e) and f) SEM images with the EDX spectrum #2 from a region with pores and spherical nano-sized features; g) EBSD investigations for the as-built sample in the z-axis for the austenite and h) ferrite - martensite phases and i) in the basal plane for the austenite and j) ferrite - martensite phases.

STEM analysis (Fig. 4a, b, c) showed the dark spherical features that decorate the matrix to be distributed inside the martensite or ferrite grains but also at the grain boundaries. Furthermore, the high-resolution STEM image of such a particle in Fig. 4d and the X-ray elemental maps and line scan in Fig. 4e, confirmed that they are indeed nanometric oxide phases containing Si, Al, Ti, Cr, Mn. Their internal structure is disordered crystalline and core-shell-like, with a core consisting mainly of silicon and a shell of titanium and chromium, while aluminum and manganese are evenly distributed. However, in some nano-oxides, the shell of titanium and chromium was found to be sheet like (probably a couple of atomic layers thick) and crystalline. While the other elements are expected, the presence of Al and Ti impurity atoms probably originates from the alloy

 doi:10.20944/preprints202111.0356.v1

ingot casting, which was subsequently converted into powder. However, their concentration seems to be high enough to form densely dispersed oxides in the matrix.

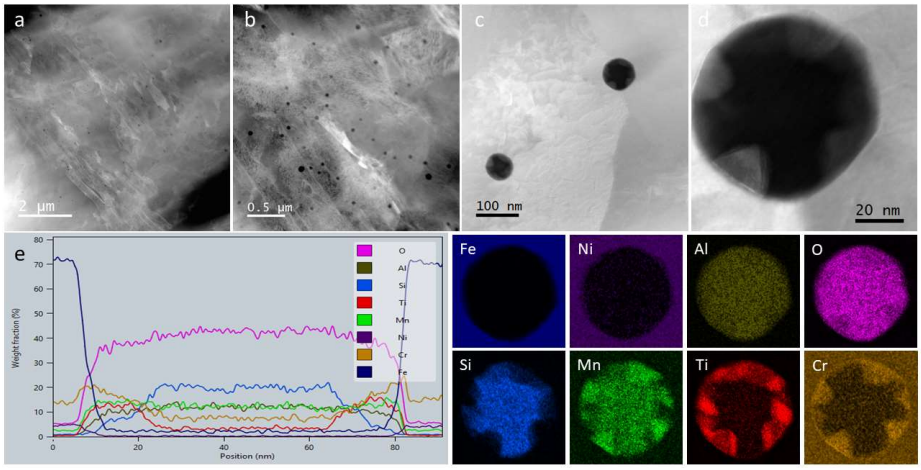

Figure 4. STEM investigations for the as-built sample. a) and b) low magnification HAADF images; c) and d) high resolution HAADF images; e) EDX line scan and EDX maps from the particle represented in d).

The thermally treated sample (1050°C / 3min / air + 620°C / 4h / air) (Fig. 5a-b) exhibits a martensitic refined microstructure. The segregations (Fig. 5c and EDX #1) at the melt pool interfaces however were not entirely dissolved. The Nb-rich carbides and the nano-oxides (Fig. 5d-f with EDX #2 and #3) are also still preserved. As expected, the typical intermetallic Ni precipitates (200 nm - 700 nm) were mainly formed at the grain or lattice boundaries.

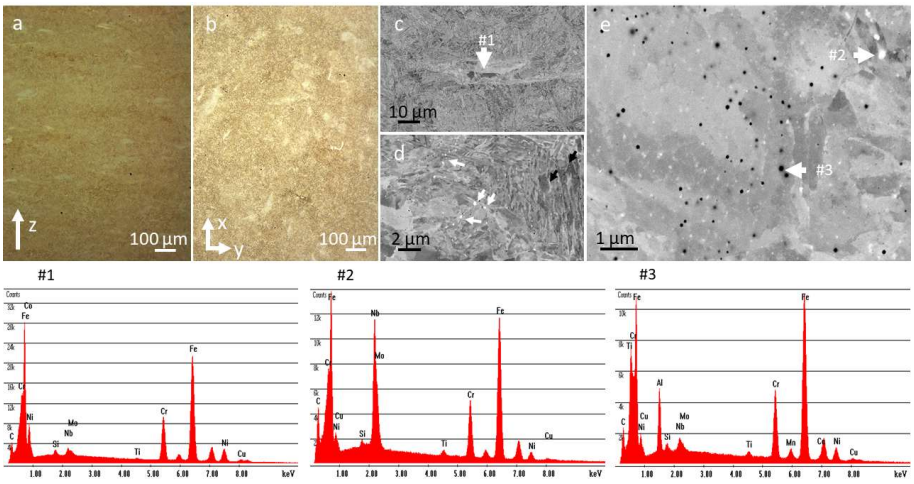

Figure 5. Thermally treated sample (1050°C / 3min / air + 620°C / 4h / air) characterization by optical microscopy and SEM. a) and b) IFM images in the z-axis and basal plane; c) and d) SEM images at low magnification with the EDX spectrum from segregation area #1; and e) higher magnification SEM image with the EDX spectra from the bright #2 and dark #3 particles.

Figures 6 and 7a present STEM HAADF images and EDX maps for areas containing both Ni-precipitates and nanoparticles (oxides and carbides) at low and high magnification, respectively. Along with the NbC and nano-oxides that have not changed their morphology or chemical composition, we found a high density of Cu nanoparticles (5 – 20 nm) uniformly distributed in the matrix. The element concentrations in the oxides

Preprints (www.preprints.org) | NOT PEER-REVIEWED | Posted: 19 November 2021 doi:10.20944/preprints202111.0356.v1

and carbides vary only slightly and can thus be considered stable phases. Exemplar line scans for the typical nanoparticles indicated by arrows on the Mn, Ti, and Nb maps in figure 6, are also shown. Both nanoparticle types, nano-oxides and nano-carbides (NbC), were not affected at all by the heat treatment at 620°C.

Nevertheless, possible nanopores partially filled with oxygen and having Cu, Mn, and Ni adsorbed on their walls are also shown in figure 7b. Their presence, however, might be induced by the electron beam affecting the nano-oxides situated closed to the surface of the very thin STEM sample.

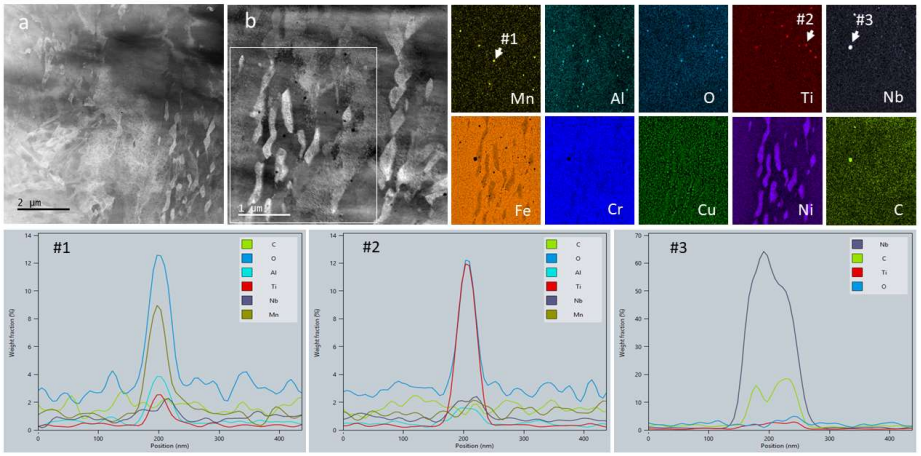

Figure 6. STEM investigations for the thermally treated sample. a) HAADF image at low magnification; b) HAADF image with the rectangle indicating the area for EDX maps. EDX line scans over particles #1 (manganese oxide), #2 (titanium oxide), #3 (niobium carbide).

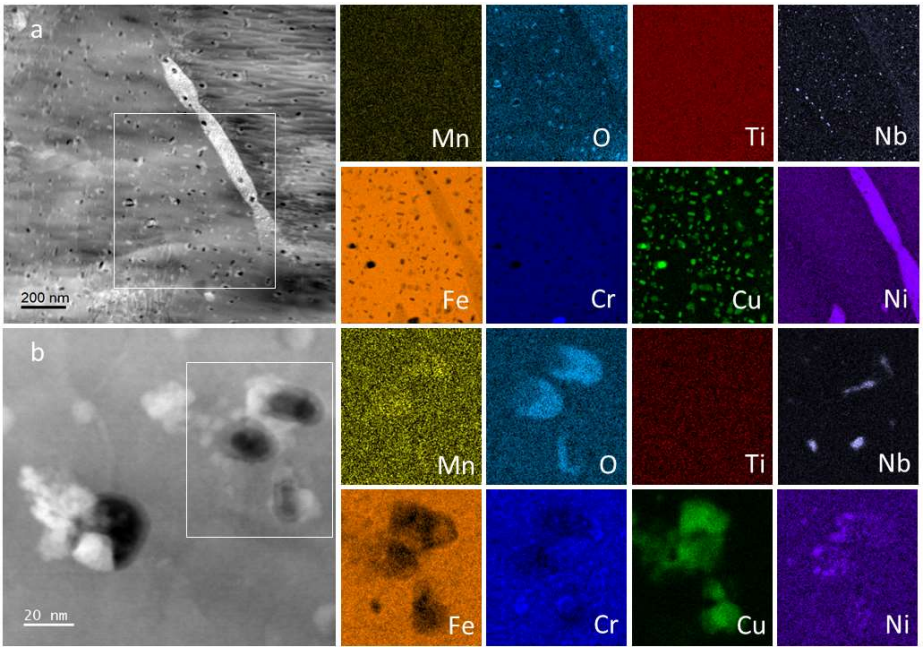

Figure 7. a) EDX maps from an area containing nanometric oxide in thermally treated sample. b) EDX maps at higher magnifications to reveal nanometric pores filed with oxygen and having Cu, Mn and Ni adsorbed on the walls.

In order to clarify whether the oxides are stable at elevated temperatures and to observe the nucleation of the nanosized Cu, Cr and Ni precipitates, we performed

Preprints (www.preprints.org) | NOT PEER-REVIEWED | Posted: 19 November 2021 doi:10.20944/preprints202111.0356.v1

simultaneous thermal analysis (STA) measurements of the as-built sample and STEM *in situ* heating experiments accompanied by EDX analyses.

With the first STA experiment the heat treatment was simulated with a heating rate of 10 K/min up to 1050°C and a dwell time of 30 minutes, followed by a rapid cooling with 50 K/min, all in Argon atmosphere (Fig. 8). The STA curve exhibits an exothermal peak at 483°C in the first heating segment followed by another broad exothermal peak above 600°C. In the cooling segment no signals were detected that would indicate a reversibility of these processes. The measurement at a higher heating rate 35 K/min (not shown here) showed a shift of the first exothermal peak toward higher temperatures (501°C).

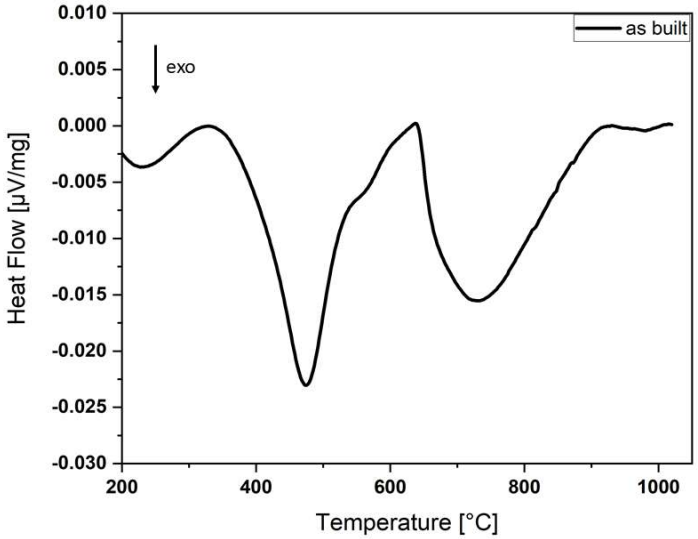

Figure 8. Simultaneous thermal analysis (STA - extracted DSC curve) measurements of the "as-built" sample at 10 K/min heating rate.

In addition, the "as-built" sample was *in situ* heated in the high-resolution microscope operated in STEM mode, starting at room temperature (23°C) up to 950°C at a heating rate of 8.6 K/min for the temperature range between 23°C and 550°C and 2.8 K/min between 550 °C and 950 °C (suppl. Fig. 1). It is worth noting that heating at a temperature above 950 °C was hindered by the fact that the matrix in the very thin lamella decomposed almost completely (Fig. 9a).

The overall appearance of the microstructure on the HAADF images seemed to remain stable up to 600°C (Fig. 9a) even though the STA measurement indicated an exothermic peak at 480°C that is related to the formation of Cu clusters and nanoparticles [21]. Nevertheless, on the high magnification EDX maps taken at 500 °C, we could indeed observe a few Cu nanoparticles (Cu map and line scan on Fig. 10). On the images acquired with the HAADF detector, however, the formation of the nanoparticles and their continuous coarsening (intermetallic Cu, Cr and Ni) was first observed above 650°C and up to 950°C. (At this point we have to note that imaging alone, also using different detectors, without analytical evidence did not deliver the complete information about the dynamic of the alloy system.) While the coarsening of Cu and Ni precipitates was rather slow, the coarsening rate for Cr precipitates proved to be higher. Moreover, we also observed the precipitation of Cr23C6, contrary to the general knowledge that in Cr containing maraging steels, Cr23C6 precipitate nucleation should be restricted due to the low carbon concentration. Phase diagrams for PH-17 stainless steel [22, 23] show a very low mass fraction for the M23C6 phase with possible coarsening above 650°C. We assume that the nucleation of the Cr23C6 precipitate during *in situ* heating (Fig. 11), is due to accelerated surface diffusion of Cr and C atoms (also probably supplied by the fixing alloy for the FIB lamella on the heating chip, which is a mixture of Pt and C) at higher

Preprints (www.preprints.org) | NOT PEER-REVIEWED | Posted: 19 November 2021 doi:10.20944/preprints202111.0356.v1

temperatures. Although we tried to minimize the contribution of the fixing alloy by preparing the FIB lamella in a window-like manner (thin middle area with very thick edges acting as barriers for diffusion), this effect could eventually not be completely prevented.

The nano-oxides, on the other hand, remained stable up to 950°C and retained their spherical morphology, complex or core-shell-like chemical composition, and crystallographic disorder. Figure 9b shows images at temperatures between 23°C and 760°C from an area at higher magnification containing few nano-oxides. Above 700°C, the matrix in this region started to decompose quickly covering some oxides. However, they are still visible at lower magnification in figure 9a. Chemical analysis of a nano-oxide was performed at room temperature and compared to the analyses at 500°C and 800°C. We did not detect any changes on the EDX maps shown in figure 10 at all three temperatures. However, the EDX maps at 800°C were recorded at lower magnification to feature the changes undergone by the matrix surrounding the nano-oxide. The high-resolution STEM images of such a particle at different temperatures presented in supplementary figure 2 show the cupper segregation in the proximity of the nano-oxide at temperatures above 600°C. The shape of the particle is slightly changed at 850°C due to the Cu and Cr segregations as well as matrix deterioration.

Figure 11 exemplifies the STEM HAADF image and chemical analyses of a large area at 700°C. The EDX maps display the coarsened Cr (about 200 nm) and Ni (larger than 250 nm) precipitates, the Cu (about 20 – 30 nm) and oxide nanoparticles, but also silicon segregations of about 2 – 5 nm at martensite lath interfaces.

a)

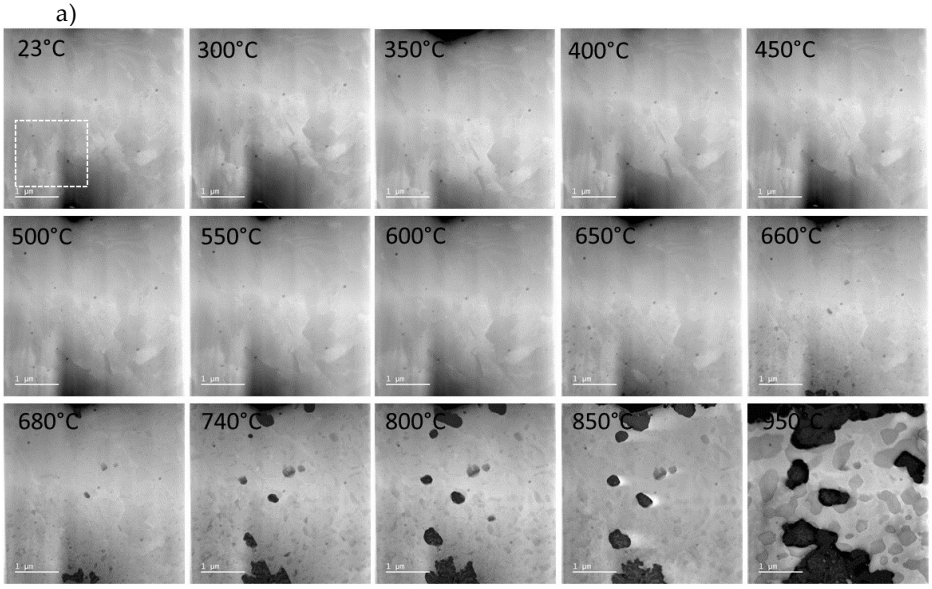

Preprints (www.preprints.org) | NOT PEER-REVIEWED | Posted: 19 November 2021 doi:10.20944/preprints202111.0356.v1

b)

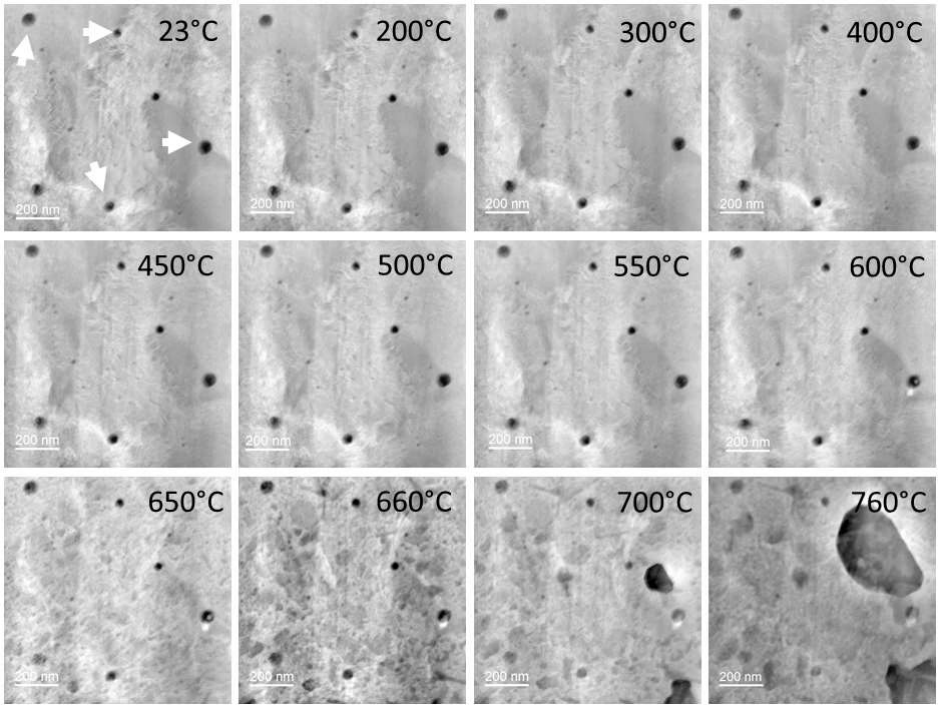

Figure 9. *In situ* heating study for the as-built sample a) at lower magnification to observe the nucleation and coarsening of the Cr- and Ni-rich precipitates, and b) at higher magnification to follow the evolution of the nanometer sized oxides.

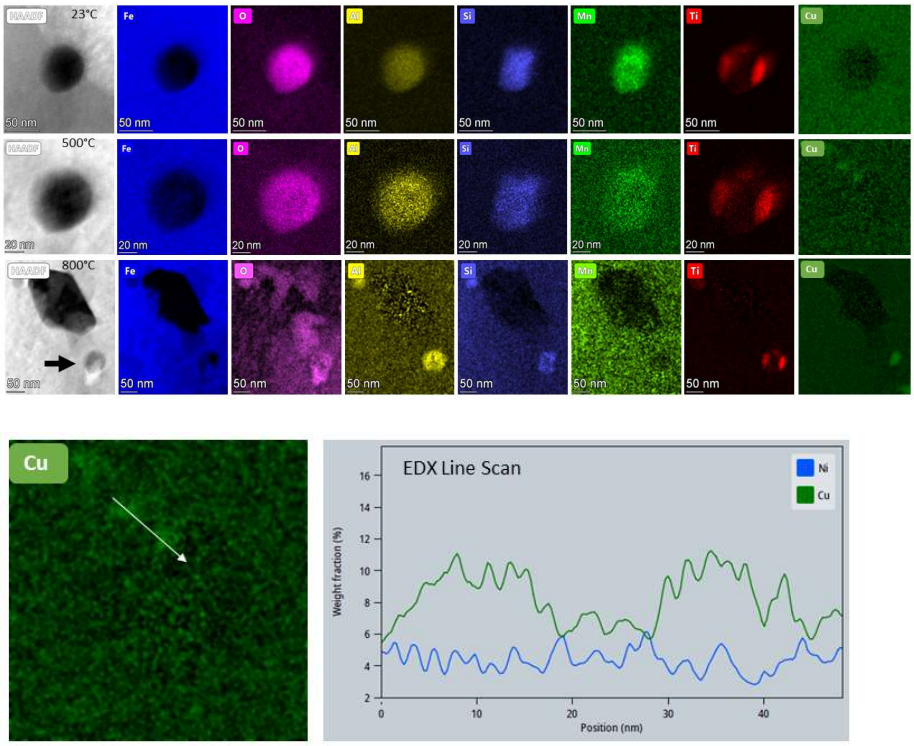

Figure 10. EDX analysis of a nanometer sized oxide in the as-built sample at room temperature (23°C), 500°C and 800°C. EDX line scan over two Cu nano-precipitates at 500°C (Ni signal on the line scan is displayed for comparison).

Preprints (www.preprints.org) | NOT PEER-REVIEWED | Posted: 19 November 2021 doi:10.20944/preprints202111.0356.v1

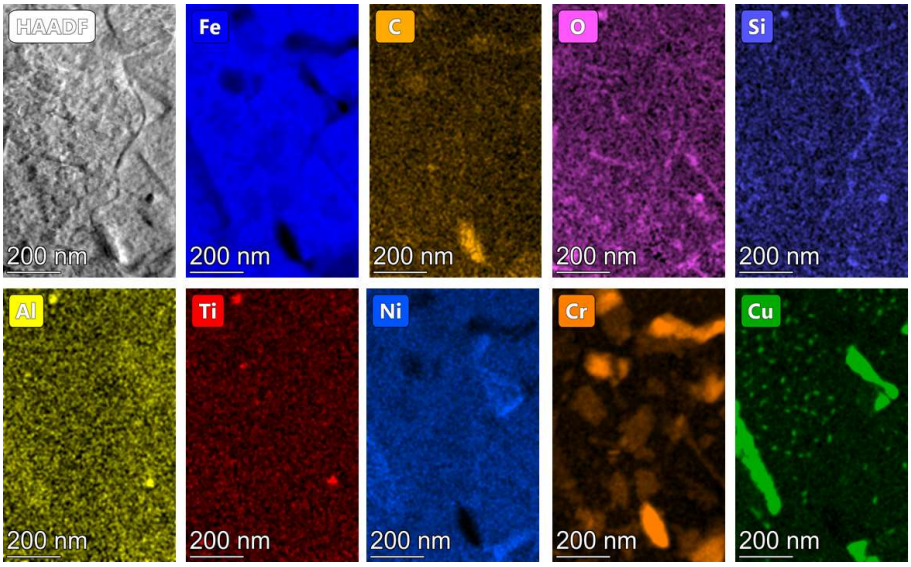

Figure 11. EDX analysis at lower magnification at 700°C.

When comparing the STA measurements with the *in situ* STEM measurements at 450°C and 500°C, we observed that the exothermic peak present at 481°C (10 K/min) or 501°C (35 K/min) do not resemble any dramatic changes in the microstructure that could be detected on the images at low magnification. At higher magnification however, the Cu-EXD map (Fig. 10) demonstrates the formation of dense Cu clusters and nanoparticles as reported in the literature for the PH 15-5 [21]. This process is probably driven by the continuous stress release that starts already at low temperatures (probably above 200°C) and pipe diffusion through dislocations. Beside pipe diffusion, the surface diffusion accelerated the growing of the Cu- nanoparticles at higher temperatures and the nucleation of Cr and Ni intermetallic precipitates followed by their coarsening that give rise to the broad exothermic peak starting at 620°C.

Therefore, we can understand the STA curve considering matrix relaxation at low temperature (below 450°C), formation of Cu clusters between 470°C and 520°C followed by coarsening until 950°C and precipitation and coarsening of Cr- and Ni particles between 620°C and 950°C. The nanosized oxides remained unchanged over the whole range of temperatures, therefore no influence on the STA curve is expected.

4. Discussion

The powder analysis confirmed the thin passive oxide layer that covered the particles and irregularities, that seems to supply sufficient oxygen to the system to ensure the formation of nano-oxides during the printing process. The nano-oxides in the as built sample can have, depending on printing parameters, a high density in the vicinity of the melt pools or be evenly distributed in the matrix.

In the thermally treated sample the nano-oxides are not affected at all by the heat treatment at 620°C (their thermal stability has also been acknowledged by Sun et al (2018)). Furthermore, the *in situ* heating experiment up to 950°C confirmed their stability in all aspects (Fig. 11) suggesting that they could be beneficial in terms of strength or creep resistance at elevated temperatures.

Very often the oxides in the as built sample have been identified as pores since micrometer sized pores with variate morphologies and nanopores are frequently present in the additively manufactured parts. While the micrometer sized are easy to detect by different macroscopic methods, in the optical and SEM microscopes or by X-ray computer tomography, the nanopores detection needs high-resolution investigation methods such as STEM images accompanied by chemical composition analyses using X-ray and electron energy loss spectroscopy (EELS). Advanced methods such as EELS fine structure (ELNES)

analysis of the oxygen edge can even distinguish between molecular oxygen (or nitrogen) in gas form and bound oxygen (carbon, nitrogen) in amorphous or crystalline state. Furthermore, this method can be applied for detection of such atoms at grain / subgrain or melt-pool boundaries.

On the other hand, the amorphous carbon found at the interfaces between the powder particle body and the envelopes (corrupted particles), added to the nominal concentration presented in Table 1, supplied sufficient carbon for niobium to form nano-carbides (NbC), but also few chromium carbides at higher temperatures as presented in Fig. 9 and 11. The NbC appear on the EDX maps (Fig. 6 and 7) and with a bright contrast on the SEM images (Fig. 5e #2) while the chromium carbides are visible only on the *in situ* heating HAADF images acquired above 660°C in Fig. 9b and on the EDX maps at 700°C in Fig. 11.

The STA curve in Figure 8 confirmed our results in the in-situ heating measurements, validating this method for the heat tempering study of other steel grades and alloys.

5. Conclusions

Correlative electron microscopy and STA investigations were performed for the X5CrNiCuNb17-4 maraging steel to better understand the microstructure characteristics and mechanical properties of the final additively manufactured parts.

Regular and irregular powder grains high resolution microstructure analyses revealed the thin copper segregations and the amorphous carbon layer as well as the surface superficial oxidation of about 10 nm.

Further, the microstructure characterization of the as-built condition unveiled the presence of nanosized oxides distributed in the matrix. These particles have been shown to persist in the thermally treated state and, together with the formation of the expected intermetallic Ni precipitates at the interfaces between the laths and the Cu nanoparticles, contribute to the improved mechanical properties of the material.

During *in situ* heating in STEM we observed the formation and coarsening of Cu nanoparticles that reached dimensions larger than 200 nm at 700°C, and precipitation of Ni and Cr particles that continuously coarsened at higher temperatures reaching 500 nm at 950°C. These observations are in line with the STA measurement at higher temperatures.

The origin of the Al, Si, Ti, Mn and Cr containing nanosized oxides already observed in the as-built sample, is most probably linked to the very thin superficial oxidation layer on the powder particles. The *in situ* heating experiment in STEM confirmed their exceptional stability up to 950°C. They preserved their dimensions, spherical morphology and chemical composition, and might be considered as strengthening particles in addition to Ni and Cu precipitates.

Consequently, we conclude that the controlled superficial oxidation of steel powder grains can in fact be reversed into an advantage, to produce oxide-dispersive strengthened additively manufactured steel parts with higher thermal stability.

Supplementary Materials: The following are available online at www.mdpi.com/xxx/s1, Figure S1, Figure S2.

Author Contributions: Conceptualization, Mihaela Albu; Data curation, Mihaela Albu; Formal analysis, Cecilia Poletti; Funding acquisition, Mihaela Albu and Gerald Kothleitner; Investigation, Mihaela Albu, Bernd Panzirsch, Hartmuth Schröttner, Stefan Mitsche and Klaus Reichmann; Methodology, Mihaela Albu; Project administration, Mihaela Albu; Writing – original draft, Mihaela Albu and Klaus Reichmann; Writing – review & editing, Mihaela Albu.

Funding: This research was funded by the Austrian Research Promotion Agency (FFG): SP2018-003-006 (Microstructure of 3D printed metallic parts).

Acknowledgments: The authors are also grateful to Martina Dienstleder for STEM specimen preparation and Robert Krisper for the preparation of the in-situ FIB Lamella, to Liang Wu for the

3D printing and thermal treatment of the investigated samples and to Horst Zunko for fruitful discussions.

Conflicts of Interest: The authors declare no conflict of interest. The funders had no role in the design of the study; in the collection, analyses, or interpretation of data; in the writing of the manuscript, or in the decision to publish the results.

References

1. Turk, C., Zunko, H., Aumayr, C., Leitner, H., Kapp, M., Advances in Maraging Steels for Additive Manufacturing, Berg Huettenmaenn Monatsh, 164(3) (2019), 112–116, https://doi.org/10.1007/s00501-019-0835-z
2. Bai, Y., Yang, Y., Wang, D., Zhang, M., Influence mechanism of parameters process and mechanical properties evolution mechanism of maraging steel 300 by selective laser melting, Mat. Sci. Eng. A, 703 (2017), 116-123, http://dx.doi.org/10.1016/j.msea.2017.06.033
3. Sedlak, J., Rican, D., Piska, M., Rozkosny, L., Study of Materials Produced by Powder Metallurgy Using Classical and Modern Additive Laser Technology, Proc. Eng. 100 (2015), 1232 – 1241, doi: 10.1016/j.proeng.2015.01.488
4. Kempen, K., Yasa, E., Thijs, L., Kruth, J.-P., Van Humbeeck, J., Microstructure and mechanical properties of Selective Laser Melted 18Ni-300 steel, Phys. Proc. 12 (2011) 255–263, doi:10.1016/j.phpro.2011.03.033
5. Bajaj, P., Hariharan, A., Kini, A., Kürnsteiner, P., Raabe, D., Jägle, E.A., Steels in additive manufacturing: A review of their microstructure and properties, Mat. Sci. Eng. A 772 (2020) 138633, https://doi.org/10.1016/j.msea.2019.138633
6. Sun, Y., Hebert, R.J., Aindow, M., Non-metallic inclusions in 17-4PH stainless steel parts produced by selective laser melting, Mater. Des. 140 (2018) 153–162, https://doi.org/10.1016/j.matdes.2017.11.063
7. Tatlock, G.J., Dawson, K., Boegelein, T., Moustoukas, K., Jones, A.R., High resolution microstructural studies of the evolution of nano-scale, yttrium-rich oxides in ODS steels subjected to ball milling, selective laser melting or friction stir welding, Mater. Today Proc. 3 (2016) 3086–3093, https://doi.org/10.1016/j. matpr.2016.09.024.
8. Gao, R., Zeng, L., Ding, H., Zhang, T., Wang, X., Fang, Q., Characterization of oxide dispersion strengthened ferritic steel fabricated by electron beam selective melting, Mater. Des. 89 (2016) 1171–1180, https://doi.org/10.1016/j. matdes.2015.10.073.
9. Springer, H., Baron, C., Szczepaniak, A., Jägle, E.A., Wilms, M.B., Weisheit, A., Raabe, D., Efficient additive manufacturing production of oxide- and nitride-dispersion-strengthened materials through atmospheric reactions in liquid metal deposition, Mater. Des. 111 (2016) 60–69, http://dx.doi.org/10.1016/j.matdes.2016.08.084
10. Wang, Y. M., et al., Additively manufactured hierarchical stainless steels with high strength and ductility, Nat. Mat. 17 (2018), 63-70, DOI: 10.1038/NMAT5021
11. Saeidi, K., Kvetkova, L., Lofaj, F., Shen, Z., Austenitic stainless steel strengthened by the in situ formation of oxide nanoinclusions, RSC Adv. 5 (2015) 20747–20750, https://doi.org/10.1039/C4RA16721J.
12. Yan, F., Xiong, W., Faierson, E., Olson, G.B., Characterization of nano-scale oxides in austenitic stainless steel processed by powder bed fusion, Scr. Mater. 155 (2018) 104–108, https://doi.org/10.1016/j.scriptamat.2018.06.011.
13. Bodziak, S., Al-Rubaie, K.S., Valentina, L.D., Lafratta, F.H., Santos, E.C., Zanatta, A. M., Chen, Y., Precipitation in 300 grade maraging steel built by selective laser melting: aging at 510°C for 2 h, Mater. Char. (2019) 73–83, https://doi.org/ 10.1016/j.matchar.2019.02.033
14. Lou, X., Andresen, P.L., Rebak, R.B., Oxide inclusions in laser additive manufactured stainless steel and their effects on impact toughness and stress corrosion cracking behavior, J. Nucl. Mater. 499 (2018) 182–190, https://doi. org/10.1016/J.JNUCMAT.2017.11.036
15. Huang, Z., Creep-resistant aeroengine shaft steels: precipitates and consequences, Mat. Sci. Tech. 35(12) (2019), 1405–1415, https://doi.org/10.1080/02670836.2019.1627500
16. Data sheet N700 AMPO, voestalpine BÖHLER Edelstahl GmbH & Co KG, www.voestalpine.com/bohler-edelstahl (accessed 01.03.2021)
17. Murayama, M., Katayama, Y., Hono, K., Microstructural Evolution in a 17-4 PH Stainless Steel after Aging at 400°C, Metallurg. Mat. Trans. A 30A (1999), 345-353
18. Sun, Y., Hebert, R.J., Aindow, M., Effect of heat treatments on microstructural evolution of additively manufactured and wrought 17-4PH stainless steel, Mater. Des. 156 (2018), 429–440, https://doi.org/10.1016/j.matdes.2018.07.015
19. Albu, M., Krisper, R., Lammer, J., Kothleitner, G., Fiocchi, J., Bassani, P., Microstructure evolution during in-situ heating of AlSi10Mg alloy powders and additive manufactured parts, Additive Manufacturing 36 (2020) 101605, https://doi.org/10.1016/j.addma.2020.101605
20. Albu, M., Mitsche, S., Nachtnebel, M., Krisper, R., Dienstleder, M., Schröttner, H., Kothleitner, G., Microstructure Investigations of Powders and Additive Manufactured Parts, Berg Huettenmaenn Monatsh 165(3) (2020), 169-174, https://doi.org/10.1007/s00501-020-00958-3
21. Primig, S. and Leitner, H., Transformation from continuous-to-isothermal aging applied on a maraging steel, Mat. Sci. Eng. A, 527 (2010), 4399-4405, doi:10.1016/j.msea.2010.03.084
22. Cheruvathur, S., Lass, E.A., Campbell, C.E., Additive Manufacturing of 17-4 PH Stainless Steel: Post-processing Heat Treatment to Achieve Uniform Reproducible Microstructure, JOM, 68 (3) (2016), 930-942, DOI: 10.1007/s11837-015-1754-4

23. Meredith, S.D., Zuback, J.S., Keist, J.S., Palmer, T.A., Impact of composition on the heat treatment response of additively manufactured 17–4 PH grade stainless steel, Mat. Sci. Eng. A, 738 (2018), 44-56, https://doi.org/10.1016/j.msea.2018.09.066